Exploring the geostrophic regime of rapidly rotating convection with experiments

Exploring the geostrophic regime of rapidly rotating convection with experiments

Hadi Rajaei, Rudie P. J. Kunnen, and Herman J. H. Clercx

Citation: Physics of Fluids **29**, 045105 (2017); doi: 10.1063/1.4980072
View online: http://dx.doi.org/10.1063/1.4980072
View Table of Contents: http://aip.scitation.org/toc/phf/29/4
Published by the American Institute of Physics

Exploring the geostrophic regime of rapidly rotating convection with experiments

Hadi Rajaei, Rudie P. J. Kunnen, and Herman J. H. Clercx
Fluid Dynamics Laboratory, Department of Applied Physics and J. M. Burgers Center for Fluid Dynamics, Eindhoven University of Technology, P.O. Box 513, 5600 MB Eindhoven, The Netherlands

(Received 23 February 2017; accepted 30 March 2017; published online 13 April 2017)

Rapidly rotating Rayleigh–Bénard convection is studied using time-resolved particle image velocimetry and three-dimensional particle tracking velocimetry. Approaching the geostrophic regime of rotating convection, where the flow is highly turbulent and at the same time dominated by the Coriolis force, typically requires dedicated setups with either extreme dimensions or troublesome working fluids (e.g., cryogenic helium). In this study, we explore the possibilities of entering the geostrophic regime of rotating convection with classical experimental tools: a table-top conventional convection cell with a height of 0.2 m and water as the working fluid. In order to examine our experimental measurements, we compare the spatial vorticity autocorrelations with the statistics from simulations of geostrophic convection reported earlier in [D. Nieves *et al.*, "Statistical classification of flow morphology in rapidly rotating Rayleigh-Bénard convection," Phys. Fluids **26**, 086602 (2014)]. Our findings show that we have indeed access to the geostrophic convection regime and can observe the signatures of the typical flow features reported in the aforementioned simulations. *Published by AIP Publishing.* [http://dx.doi.org/10.1063/1.4980072]

I. INTRODUCTION

Rotating Rayleigh–Bénard convection (RRBC), a layer of fluid heated from below and cooled from above while rotating about a vertical axis, is a classical system to model various geophysical and astrophysical flows, e.g., liquid metal cores of terrestrial planets, rapidly rotating stars, and Earth's ocean currents.[1–3] These systems satisfy two conditions: they are highly turbulent and at the same time dominated by the Coriolis force. Maintaining high levels of turbulence while the flow is rotationally constrained imposes severe difficulties in both experiments and simulations. In experiments it is exceedingly hard to maintain a rotation-dominated flow without enacting significant centrifugal buoyancy. The limitations on the simulations arise from the enormous range of (physical and temporal) scales to be resolved: Ekman-type boundary layers near no-slip plates in a rotating fluid are typically very thin and waves in such rotating fluids require small time steps in simulations. These limitations to the numerical solution of the full incompressible Navier–Stokes equations (in the Boussinesq approximation) in the rapidly rotating limit have led Julien and co-workers to formulate a set of asymptotically reduced equations in the limit $Ro \to 0$, where Ro is the Rossby number, the ratio of inertial and Coriolis forces.[4,5] While these asymptotically reduced equations neglect the Ekman boundary layer and fast inertial waves, the gain is huge. Therefore, these equations have been widely used to characterize the flow morphologies from the onset of convection to geostrophic turbulence.[5–10] Very recently, Ekman pumping effects are also incorporated in these equations, see Refs. 11 and 12.

At small enough Ro, experiments and direct numerical simulations (DNSs) of the full Navier–Stokes equations (in the Boussinesq approximation) should give similar results as simulations of the asymptotically reduced equations. Up to now, most of the experiments[13–23] and DNSs[16,18,24–27] did not reach deep into the rapidly rotating convection regime. The few experimental and numerical studies that entered decisively into this regime[9,28–30] primarily use the overall heat transfer to characterize rapidly rotating Rayleigh–Bénard convection and identify transitions between flow regimes from changes in the heat-flux scaling. These findings suggest a phase diagram as sketched in Figure 1, with the Ekman number Ek indicating the ratio of viscous forces over Coriolis forces and the strength of thermal forcing is quantified by the Rayleigh number Ra and normalized by its critical value Ra_{cr} for the onset of convective motion. Ra_{cr} grows as the rotation rate is increased.[31] Different turbulent regimes can be identified: (I) the rotation-unaffected regime where large scale circulation is the main feature of the flow and the heat flux remains constant; (II) the rotation-affected regime where rotation-aligned vortical plumes characterize the flow and the heat flux increases with increasing background rotation (for $Pr > 1$, where Pr is the Prandtl number; it specifies the diffusive properties of the fluid); and (III) the geostrophic regime where the flow is principally governed by a balance of the Coriolis force and the pressure gradient force and the heat flux drops dramatically with increase in the background rotation. In Figure 1, the dashed and solid black lines indicate the transitions to the rotation-affected and the geostrophic regimes, respectively, for $Pr = 0.7$, see Ref. 28. The two gray dashed lines indicate the proposed alternative predictions for the transition to the geostrophic regime suggested by Ref. 16 (upper gray dashed line, for $Pr \approx 7$) and Ref. 32 (lower gray dashed line, for $Pr \approx 4.5 - 11$). The dotted line is the lower bound of the geostrophic regime ($Ra/Ra_{cr} \simeq 3$, see Ref. 28), below which linear or chaotic convection is expected. The filled blue

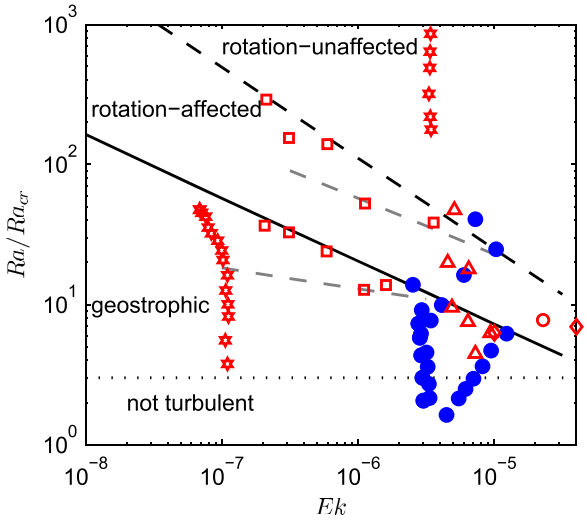

FIG. 1. Phase diagram of rotating convection as proposed by Ref. 28. The transition between rotation-unaffected regime and rotation-affected regime (for $Pr = 0.7$, obtained from heat-transfer measurements in cryogenic helium and given by $Ra = 0.086Ek^{-2}$) is indicated by the dashed black line.[28] The aforementioned transition for $Pr \approx 6$ is out of the graph, given by $Ra = 24Ek^{-2}$, see Ref. 28. The solid black line, given by $Ra = 0.25Ek^{-1.8}$, is the proposed crossover to the geostrophic regime for $Pr = 0.7$. The two gray dashed lines are the alternative predictions of the transition to the geostrophic regime suggested by Refs. 16 and 32. These lines are given by $Ra = 1.4Ek^{-7/4}$ (upper dashed line, for $Pr \approx 7$) and $Ra \approx 10Ek^{-3/2}$ (lower dashed line, for $Pr \approx 4.5 - 11$), respectively. The dotted black line indicates the transition to a regime of linear or chaotic convection at $Ra/Ra_{cr} \simeq 3$ as proposed by Ref. 28. The filled blue circles are for the current experiments with $Pr \approx 6 - 8$. The open red symbols are the literature data; diamonds from Ref. 16, circles from Ref. 17, upright triangles from Ref. 20, squares from Ref. 28, and stars from Ref. 29.

and open red symbols correspond to the current experimental data and the data from the literature, respectively.[16,17,20,28,29] Red symbols are further explained in the caption of Figure 1. Note that the transition between the rotation-unaffected and rotation-affected regimes in Figure 1 (dashed black line) is plotted for $Pr = 0.7$. This transition strongly depends on Pr and the corresponding transition for $Pr \simeq 7$ (similar to Pr number in our experimental data) is vertically above the axis limits of Figure 1. On the other hand, the transition between the rotation-affected and the geostrophic regimes, which is of interest in this study, is reported to be less affected by Pr, see Ref. 28.

The experiments that conclusively reached the geostrophic regime are highly dedicated setups with either lack of optical access[28] (red open squares in Figure 1) or extreme dimensions[29] (red open stars in Figure 1). In Ref. 28 cryogenic helium gas near its critical point at 5.2 K is used as the working fluid and in Ref. 29 a 1.6 m tall convection cell is used compared to commonly used 0.2–0.4 m tall convection cells. Only qualitative flow visualizations have been performed in Ref. 29. The commonly used convection cells and rotating tables can reach Ekman values down to approximately 3×10^{-6}, allowing for a small part of the geostrophic regime to be accessible. In this paper we want to push our setup to the limit of rapid rotation at correspondingly chosen Rayleigh numbers to assess whether we can explore the geostrophic regime and use optical flow diagnostics to obtain statistics of the flow features to compare to the results from the asymptotic simulations. A favorable comparison is certainly not guaranteed, given the difference in boundary conditions (no-slip for experiments and stress-free for the asymptotic simulations) as well as the unavoidable centrifugal effect in experiments that prevents the application of very large rotation rates. Nevertheless, we achieve a surprisingly favorable agreement.

The simulations of the asymptotic equations have revealed four distinct flow structures, namely, cellular convection, convective Taylor columns (CTCs), plumes, and geostrophic-turbulence.[5,8,9] The cellular state occurs just above the onset of convection; it is characterized by densely packed thin hot and cold columns spanning the entire vertical extent of the flow domain. Departing from the onset of convection (Ra increases), these cells may develop into well-separated vertically aligned vertical convective Taylor columns (CTCs), surrounded by shields of vorticity of opposite sign. Another mode of convection consists of plumes with less vertical coherence and no shields. A final state is called "geostrophic-turbulence," where the vertical coherence is lost almost completely and the interior is fully turbulent. Note that all four convection modes are part of the geostrophic regime, which should thus not uniquely be identified with the geostrophic-turbulence state alone. The occurrence of these four states is strongly dependent on the Prandtl number Pr: at lower $Pr \lesssim 3$ no Taylor columns are formed, while the geostrophic-turbulence state remained out of reach for $Pr \gtrsim 7$ in the simulations.[6]

Nieves *et al.*[8] have reported earlier that the spatial autocorrelations of temperature, calculated from simulations of the asymptotically reduced equations, can be employed to differentiate between these different states. They also mention that for that purpose one could also use vertical vorticity or vertical velocity; the results should be almost identical (see also Ref. 5). We shall use vertical vorticity as a proxy for temperature.

The remainder of the paper is organized as follows. The experimental parameters are given in Sec. II A. The experimental setup and the measurement techniques are discussed in Sec. II B. In Sec. III A, the results of the spatial autocorrelation of the vertical vorticity are discussed. Next, the flow coherence along the axis of rotation is discussed in Sec. III B. We discuss our main findings in Sec. IV.

II. EXPERIMENTAL TECHNIQUES AND PARAMETERS

A. Experimental parameters

Rotating Rayleigh–Bénard convection is characterized by three nondimensional parameters, namely, the Rayleigh number Ra, the Prandtl number Pr, and the Ekman number Ek. These parameters are defined as

$$Ra = \frac{g\beta\Delta T H^3}{\nu\kappa}, \tag{1}$$

$$Pr = \frac{\nu}{\kappa}, \tag{2}$$

$$Ek = \frac{\nu}{2\Omega H^2}. \tag{3}$$

In these definitions, g is the gravitational acceleration, β is the thermal expansion coefficient of the fluid, ΔT is the applied

temperature difference, Ω is the rotation rate, ν is the kinematic viscosity of the fluid, κ is the thermal diffusivity of the fluid, and H the cell height. The Rossby number, Ro, is also widely used in rotating Rayleigh–Bénard convection and is defined as

$$Ro = \frac{\sqrt{\beta g \Delta T / H}}{2\Omega} = \sqrt{\frac{Ra}{Pr}} Ek. \quad (4)$$

The importance of the centrifugal buoyancy can be assessed by the Froude number, defined as

$$Fr = \frac{\Omega^2 R}{g}, \quad (5)$$

where R is the radius of the convection cell.

Chandrasekhar[31] used a linear stability analysis to demarcate the onset of convection and he found that $Ra_{cr} \simeq 8.6956 Ek^{-4/3}$ for small values of Ek, where Ra_{cr} is the Rayleigh number at the onset of convection, below which the flow halts and diffusion is the only active way of heat transfer. The value $RaEk^{4/3}$ is thus a similar parameter to Ra/Ra_{cr} that is used to specify the distance to Ra_{cr}. We shall use $RaEk^{4/3}$ to indicate the supercriticality, keeping in mind that $RaEk^{4/3} \simeq 8.6956$ marks the onset of convection.

Approaching the onset of convection can be achieved either by variation of the background rotation (Ω) or by variation of the temperature difference (ΔT). In the present study, both approaches have been examined and compared.

B. Experimental setup

The experimental setup consists of a cylindrical convection cell (aspect ratio, $\Gamma = 1$ and cell height, $H = 0.2$ m) and a camera system. The cylindrical convection cell, the same as the one used in Refs. 33–36, consists of a copper heating plate at the bottom, a transparent cooling chamber at the top, and a Plexiglas cylindrical vessel connecting the bottom to the top. The cylindrical vessel is placed inside a cubic box and the intervening region is filled with the same fluid as the working fluid, water, in order to minimize the distortion of the light source. A detailed description of the convection cell is provided in Refs. 35 and 36. Two different experimental techniques are used; time-resolved two-dimensional particle image velocimetry (PIV) and three-dimensional particle tracking velocimetry (3D-PTV). The 3D-PTV data provide information at different vertically distributed horizontal planes along the axis of rotation, while PIV data provide information only at one horizontal plane but at higher spatial resolution and an extended planar view.

For PIV measurements a charge-coupled device (CCD) camera (MegaPlus ES2020, 1600×1200 pixels) is placed above the cylindrical cell. The camera is equipped with a 50 mm lens. The illumination is provided by a Nd:YAG laser (Quantel CFR400) with a dominant wavelength of 532 nm. Negative cylindrical and positive lenses are used to achieve a laser sheet with a thickness of less than 1 mm. The camera and the laser are triggered by an external function generator at a frequency of 15 Hz. PIV polyamide seeding particles (density $\rho_p = 1030$ kg/cm^3, diameter $d_p = 30$–70 μm) are used.

For 3D-PTV measurements, four CCD cameras (the same camera as used for PIV), located above the cell, record the flow field. Four arrays of light-emitting diodes (LEDs) with a dominant wavelength of 455 nm illuminate a volume of $80 \times 60 \times 50$ mm^3 (x, y, z). The cameras and LEDs are triggered by a function generator at a frequency of either 15 Hz or 30 Hz, depending on the flow field. Fluorescent polyethylene particles (density $\rho_p = 1002$ kg/cm^3, diameter $d_p = 75$–90 μm) are used as tracer particles. The details of the 3D-PTV system are given in Refs. 35 and 36.

The PIV experiments are performed in a horizontal planar cross section at $z = 0.8H$, where the bottom plate is at $z = 0$.

TABLE I. Details of the PIV data sets. In the table, T_{max} and T_{min} are the hot and cold plate temperatures, respectively, L_c is the critical length (defined as $L_c = 4.8154 Ek^{1/3}$, see Ref. 31), T_b is the buoyancy time scale defined as $T_b = T_v((Ra - Ra_{cr})Ek^{4/3}/Pr)^{-1/2}$, where T_v is the viscous time scale, $T_v = (Ek^{1/3}H)^2/\nu$. The definitions of T_b and T_v are taken from Ref. 8. Viscosity and thermal diffusivity are evaluated at the mean temperature; different mean temperatures thus lead to minor variations in the parameter values such as, the Ekman number.

	$RaEk^{4/3}$	Ω (rad/s)	T_{max} (°C)	T_{min} (°C)	Ro	Pr	$Ek \times 10^6$	$Ra_{cr} \times 10^{-8}$	$Ra \times 10^{-8}$	Fr	L_c (mm)	T_b (s)
Temperature changes	18	4.12	22	18.5	0.023	7.01	3.02	1.99	4.1	0.17	13.93	7.38
	19	4.12	18.5	14	0.023	7.85	3.35	1.74	3.74	0.17	14.44	7.18
	24	4.12	19.5	14	0.026	7.74	3.31	1.76	4.78	0.17	14.34	5.88
	26	4.12	23.5	18.5	0.028	6.88	2.97	2.03	6.1	0.17	13.85	5.31
	32	4.12	21	14	0.03	7.58	3.24	1.81	6.50	0.17	14.25	4.76
	39	4.12	25.5	18.5	0.034	6.71	2.91	2.10	9.1	0.17	13.74	4.09
	40	4.12	22.5	14	0.034	7.43	3.18	1.85	8.41	0.17	14.17	4.0
	50	4.12	27.5	18.5	0.039	6.53	2.84	2.16	12.5	0.17	13.64	3.40
	63	4.12	29.5	18.5	0.044	6.36	2.77	2.23	16.3	0.17	13.53	2.95
	80	4.12	29	14	0.049	6.79	2.94	2.07	18.9	0.17	13.80	2.62
Rotation changes	14	2.75	21.6	20	0.023	6.91	4.47	1.18	1.92	0.08	15.86	12.37
	19	2.25	21.6	20	0.029	6.91	5.47	0.90	1.92	0.05	16.98	10.56
	22	2	21.6	20	0.032	6.91	6.15	0.77	1.92	0.04	17.64	9.95
	27	1.75	21.6	20	0.037	6.91	7.03	0.65	1.92	0.03	18.45	9.45
	32	1.5	21.6	20	0.043	6.91	8.20	0.53	1.92	0.02	19.42	9.03
	41	1.25	21.6	20	0.052	6.91	9.48	0.41	1.92	0.02	20.64	8.68
	55	1	21.6	20	0.065	6.91	12.30	0.31	1.92	0.01	22.23	8.4

TABLE II. Details of the 3D-PTV data sets; see the caption of Table I for more details.

	$RaEk^{4/3}$	Ω (rad/s)	T_{max} (°C)	T_{min} (°C)	Ro	Pr	$Ek \times 10^6$	$Ra_{cr} \times 10^{-8}$	$Ra \times 10^{-8}$	Fr	L_c (mm)	T_b (s)
Temperature changes	18	4.12	22	18.5	0.023	7.01	3.02	1.99	4.1	0.17	13.93	7.38
	26	4.12	23.5	18.5	0.028	6.88	2.97	2.03	6.1	0.17	13.85	5.31
	39	4.12	25.5	18.5	0.034	6.71	2.91	2.10	9.1	0.17	13.74	4.09
	50	4.12	27.5	18.5	0.039	6.53	2.84	2.16	12.5	0.17	13.64	3.40
	63	4.12	29.5	18.5	0.044	6.36	2.77	2.23	16.3	0.17	13.53	2.95
	120	4.12	37.5	18.5	0.062	5.76	2.53	2.52	34.9	0.17	13.13	2.02
Rotation changes	54	4.12	27	17	0.041	6.7	2.9	2.10	13.0	0.17	13.74	3.27
	67	3.5	27	17	0.048	6.7	3.42	1.69	13.0	0.13	14.51	3.21
	85	2.91	27	17	0.057	6.7	4.11	1.31	13.0	0.09	15.43	3.16
	142	2	27	17	0.0083	6.7	5.98	0.80	13.0	0.04	17.49	3.01
	183	1.65	27	17	0.1	6.7	7.25	0.32	13.0	0.03	18.64	3.07
	212	1	31	26	0.13	5.68	10.30	0.38	9.43	0.01	20.97	3.84

The volumetric PTV experiments cover a volume between $z = 0.76H$ and $z = 0.96H$. For both PIV and 3D-PTV measurements, the center of the measurement domain coincides with the axis of rotation. The details of the experimental parameters, conducted by PIV and 3D-PTV, are summarized in Tables I and II, respectively.

C. Data validation

3D-PTV naturally provides the data in the Lagrangian frame of reference. However, here we are interested in variables in the Eulerian frame of reference. Therefore, interpolation on a regular grid is inevitable. In the current experimental 3D-PTV data, an average number of 2700 randomly distributed particles are tracked at each time step. The particle velocity along a trajectory is calculated using a second-order finite difference method. Then, the velocities of these randomly distributed particles are interpolated (triangulation-based linear interpolation) on a regular grid with 3 mm grid spacing. Interpolation acts as a filter, consequently some (high-frequency, small-scales) information might not pass through the interpolation. We examine the effects of the interpolation on our 3D-PTV data by comparison of the interpolated 3D-PTV data and the spatially resolved PIV data as an *a posteriori* check. A comprehensive discussion of the physical interpretation of the spatial vorticity autocorrelations is given in Sec. III A; however, here we are only focused on the (dis)similarities between PIV and 3D-PTV data. Figures 2(a) and 2(b) show the spatial vorticity autocorrelations from PIV and 3D-PTV for two experiments at $RaEk^{4/3} = 18$ and 63, respectively. Each point in the plot is equidistant from the neighboring points and its distance represents the grid spacing (spatial resolution) of each technique. It is also clear from Figures 2(a) and 2(b) that PIV has a considerably higher spatial resolution compared to 3D-PTV and thus it is considered as a benchmark to validate the 3D-PTV data. The horizontal bars indicate the uncertainty as a function of the separation distance, d. Note that the uncertainty grows with d due to the accumulation of errors. The deviation for $RaEk^{4/3} = 18$ is larger than that of $RaEk^{4/3} = 63$. Note that the flow motion is considerably slower (more stable) for $RaEk^{4/3} = 18$ compared to $RaEk^{4/3} = 63$. Hence, minor imperfections (e.g., the differences in the ambient temperature for two different sets of the experiment) have a greater impact on the reproducibility of the data for $RaEk^{4/3} = 18$, thus the deviations between 3D-PTV data and PIV data might come from the reproducibility of the data. However, as can be seen from the graph, the deviations are well within the uncertainty range for both $RaEk^{4/3} = 18$ and 63. It is concluded that the interpolated 3D-PTV data have sufficient quality for the purpose of this study.

III. RESULTS AND DISCUSSION

Throughout this paper, the terminology "vorticity" is used to refer to the "vertical component of the vorticity vector." We start with a qualitative analysis of the flow field. Figures 3(a)–3(c) show snapshots of the vorticity field from

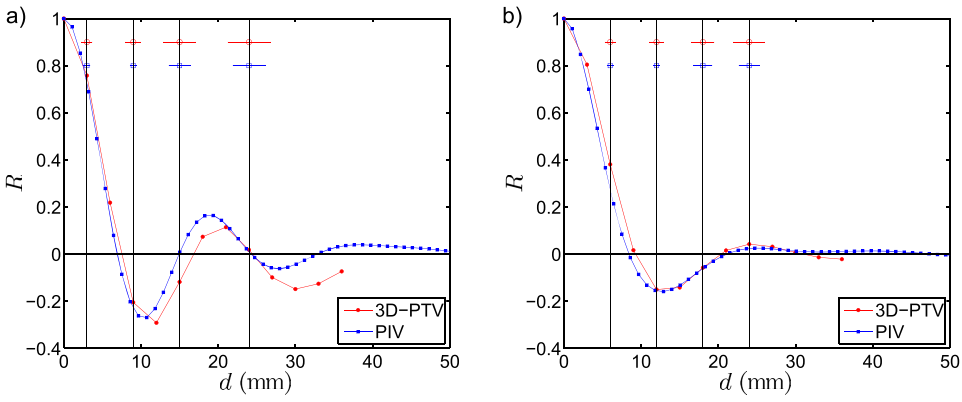

FIG. 2. The spatial vertical vorticity autocorrelation from PIV and 3D-PTV data for (a) $RaEk^{4/3} = 18$ and (b) $RaEk^{4/3} = 63$. The points on each curve are equidistant from the neighbouring points and their distances represent the spatial resolution of each technique. The horizontal bars indicate the uncertainty as a function of the separation distance, d. The uncertainty grows with d due to accumulation of the errors.

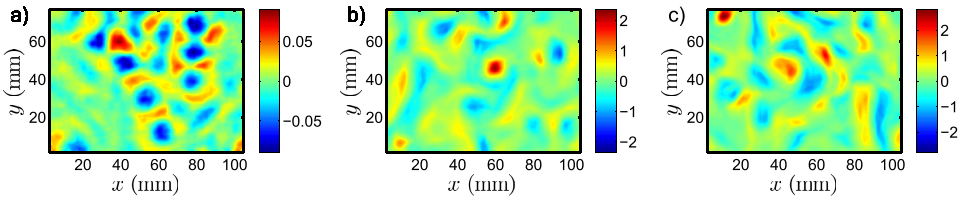

FIG. 3. The vorticity field from PIV measurements for (a) $RaEk^{4/3} = 18$, (b) $RaEk^{4/3} = 50$, and (c) $RaEk^{4/3} = 80$. The vertical and horizontal axes are in mm and the color bar is in units of 1/s.

PIV measurements at $RaEk^{4/3} = 18$, 50, and 80 (note the differences in the color bar ranges). Figure 3(a) can be identified as the cellular state; it is very similar to Figure 1(a) in Ref. 8. Note that the figure in Ref. 8 is a planar rendering of the temperature with an area of size $20L_c \times 20L_c$, while Figure 3(a) in this paper shows a planar view of the vorticity in a much smaller region ($\sim 7L_c \times 6L_c$). Judging from these plots, the transition from the cellular state to the plume state is a gradual one. The columnar state, which is represented by well separated convective Taylor columns, is not fully developed in Figure 3(b). However, the plume state is apparent for $RaEk^{4/3} = 80$, see Figure 3(c) (see also Figure 1(c) in Ref. 8). In Secs. III A and III B, a quantitative analysis based on the vorticity autocorrelation is given.

A. Spatial vorticity autocorrelation at $z = 0.8H$

The spatial vorticity autocorrelation provides information on the size of the coherent structures. The spatial autocorrelation of the vorticity in the x direction is given by

$$R^x_\omega(d) = \frac{\langle \omega(x,y,z)\omega(x+d,y,z)\rangle}{\langle \omega^2(x,y,z)\rangle}, \qquad (6)$$

where ω is the vorticity and d is the separation distance. Due to the symmetry imposed by the cylindrical cavity, we define the horizontal autocorrelation as the average of the spatial autocorrelations in the x and y directions, thus $R^{xy}_\omega(d) = \frac{1}{2}\left(R^x_\omega(d) + R^y_\omega(d)\right)$. Since $R^x_\omega(d) \simeq R^y_\omega(d)$ the averaging only results in a better convergence of the data while it does not affect any of the conclusions.

Figure 4(a) shows the spatial autocorrelations of the vorticity for some of the experiments at $z = 0.8H$, see Table I for more details. The spatial vorticity autocorrelation is found to decorrelate with itself within $d \simeq 0.8L_c$ ($L_c = 4.8154Ek^{1/3}$) and it shows a persistent negative loop (anti-correlation). The negative loop is stronger for smaller values of $RaEk^{4/3}$ (closer to the onset of convection). The negative loop is an indication that each vorticity patch is shielded by fluid with an opposite signed vorticity acting like a blanket at small $RaEk^{4/3}$ values. The shields prevent vortex-vortex interactions.[5]

As mentioned before the autocorrelations of the vertical vorticity, vertical velocity, and temperature are almost identical, see Refs. 5 and 8. Therefore, we compare vorticity autocorrelations from the experiments with temperature autocorrelations from the simulations. Figure 4(b) shows the spatial temperature autocorrelation, taken from Ref. 8. Experiments and simulations show a wavy autocorrelation for small $RaEk^{4/3}$ values. The wavy behavior is strongly suppressed for larger values of $RaEk^{4/3}$. The strength of the negative loop decreases with increase in $RaEk^{4/3}$ which indicates that the shield becomes weaker with increasing $RaEk^{4/3}$ in both experiments and simulations. However, in the simulations the negative loop disappears at $RaEk^{4/3} = 140$ (geostrophic-turbulence state). The experimental data cover a wide range of $RaEk^{4/3}$ between 14 and 212; however, the anti-correlation is always present in the experimental data. This dissimilarity between experiments and simulations is owing to the fact that the simulation at $RaEk^{4/3} = 140$ (geostrophic-turbulence state) is performed for $Pr = 1$, while in the experiments Pr is approximately 6. Julien *et al.* reported that larger values of Pr postpone the transition to the geostrophic-turbulence state.[6] In fact, these authors found a plume state for $RaEk^{4/3} = 160$ at $Pr = 7$. Therefore, it is expected that the experiments are still in the plume state even for the largest value $RaEk^{4/3} = 212$ applied here.

A more quantitative comparison between experiments and simulations is drawn by examining the half-width, the first zero crossing, the position of the minimum, the second zero crossing, and the position of the local maximum of the spatial vorticity autocorrelation. The experimental values are plotted in Figure 5 as a function of $RaEk^{4/3}$. The filled and open symbols correspond to the PIV and the 3D-PTV measurements, respectively. It is observed that the spatial vorticity autocorrelation becomes wider with increasing $RaEk^{4/3}$,

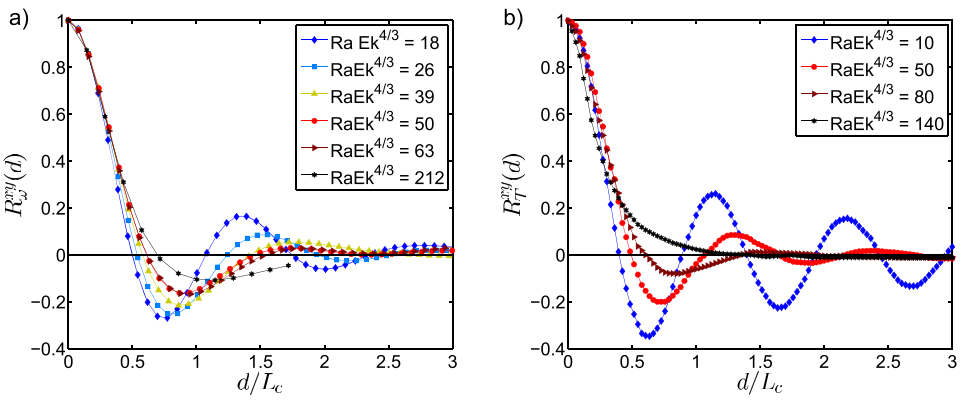

FIG. 4. (a) The spatial autocorrelation of the vorticity for different $RaEk^{4/3}$ from the experiments and (b) the spatial autocorrelation of temperature for different $RaEk^{4/3}$, taken from Ref. 8. The horizontal axis is nondimensionalized by the critical length scale, $L_c = 4.8154Ek^{1/3}$.

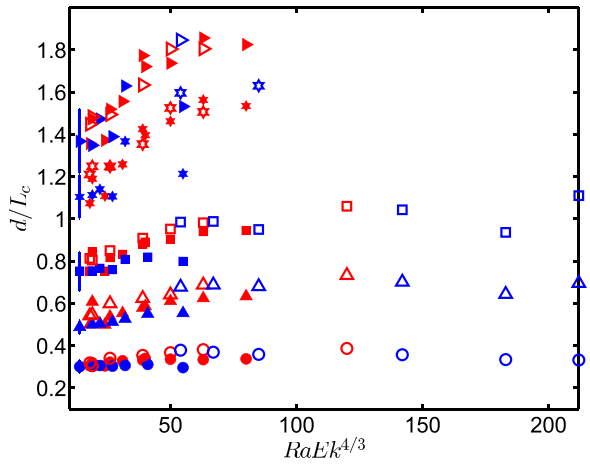

FIG. 5. The half-width (circles), the first zero crossing (upright triangles), the position of the minimum (squares), the second zero crossing (stars), and the position of the local maximum (right-pointing triangles) of the spatial vorticity autocorrelations as a function of $RaEk^{4/3}$. The open symbols are the data from 3D-PTV and filled symbols are the data from PIV. The red and blue symbols represent the experiments with variation in the temperature difference and variation in the background rotation, respectively.

e.g., the rate at which the half-width increases with $RaEk^{4/3}$ is less than that of the second zero crossing. The same result for the spatial temperature autocorrelation is observed from simulations in Ref. 8. Our experimental dataset does not contain the second zero crossing and the local maximum for $RaEk^{4/3} \gtrsim 85$ due to the fact that the structures become wider and wider with increase in $RaEk^{4/3}$ and at some point they become so large that the second zero crossing is beyond the observation view of the cameras. The extrapolation of the data reveals that the second zero crossing should keep increasing with $RaEk^{4/3}$ (e.g., the estimated second zero crossing value for $RaEk^{4/3} = 212$ is at $d/L_c \sim 2.1$).

The half-width (circles), the first zero crossing (upright triangles), the minimum (squares), and the second zero crossing (stars) from the vorticity autocorrelations are plotted again in Figures 6(a)–6(d), complimented by the same quantities obtained from temperature autocorrelations from simulations of the asymptotically reduced equations (the black solid curves). The simulation data are smaller than the experimental data. However, it should be emphasized that a one by one comparison between experiments and simulations is not the purpose and probably not even legitimate since simulations are performed for stress-free boundary conditions. Additionally, they are formally only valid for the limiting case $Ro \to 0$, though Stellmach *et al.*[9] found that the results of simulations of the asymptotic equations are still consistent with results from full Navier–Stokes DNS for $Ek \lesssim 10^{-7}$. Furthermore, the experimental data show the spatial vorticity autocorrelation while the simulations are for the spatial temperature autocorrelation. Therefore, we are more interested in the general trends rather than the actual values. From Figures 6(a)–6(d), it can be seen that the half-width, the first zero crossing, the position of the minimum, and the second zero crossing show similar trends as those of the simulations, but at generally larger values of d/L_c.

Continuing with the spatial vorticity autocorrelation, the autocorrelation coefficient values of the minimum ($R^{xy}_{\omega,min}$) and first local maximum ($R^{xy}_{\omega,max}$) as a function of $RaEk^{4/3}$ are presented in Figures 7(a) and 7(b). The solid black lines in Figures 7(a) and 7(b) are guides to the eye through the data points for $RaEk^{4/3} \lesssim 70$ and $RaEk^{4/3} \gtrsim 70$. The dashed black lines indicate $RaEk^{4/3} = 70$. The minimum values, see Figure 7(a),

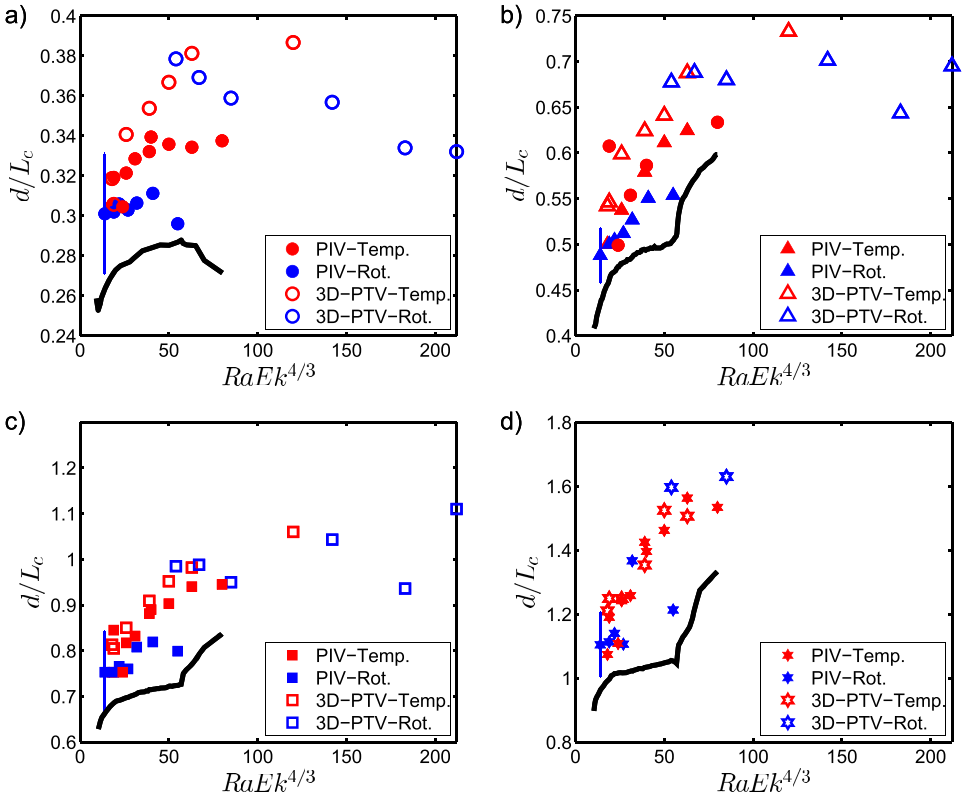

FIG. 6. (a) The half-width, (b) the first zero crossing, (c) the minimum, and (d) the second zero crossing of the spatial vorticity autocorrelation as a function of $RaEk^{4/3}$. The black curves are the corresponding values for the autocorrelations of temperature from simulations of the asymptotic equations.

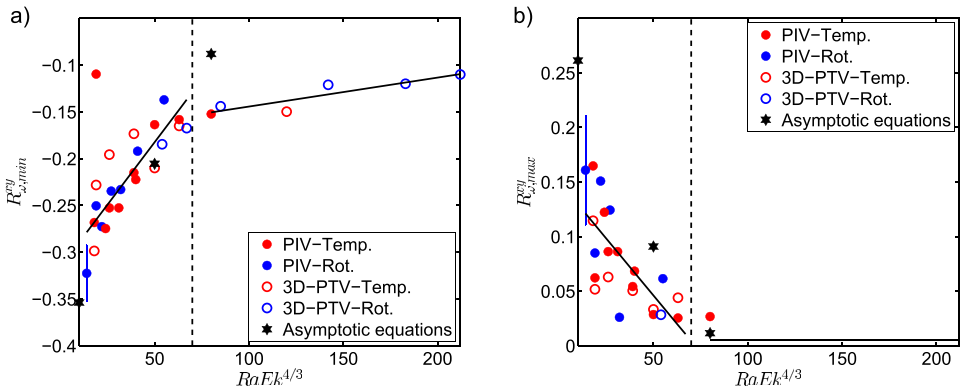

FIG. 7. (a) The minimum ($R^{xy}_{\omega,min}$) and (b) first local maximum ($R^{xy}_{\omega,max}$) of the spatial vorticity autocorrelation as a function of $RaEk^{4/3}$. The values for the asymptotic equations are taken from the spatial temperature autocorrelations. The dashed black lines are located at $RaEk^{4/3} = 70$ and the solid black lines are guides to the eye through the experimental data points for $RaEk^{4/3} \lesssim 70$ and $RaEk^{4/3} \gtrsim 70$.

approach zero with increasing $RaEk^{4/3}$. The rate at which the minimum values change is larger for $RaEk^{4/3} \lesssim 70$ than that for $RaEk^{4/3} \gtrsim 70$. The data from simulations are also plotted in the figure (black stars) with a good quantitative agreement. Note that it is expected that the anti-correlation disappears for the geostrophic-turbulence state thus the minimum value is non-existent in this state. Therefore, there is no value reported for $RaEk^{4/3} = 140$ (geostrophic-turbulence state) from simulations. As discussed before, our experimental measurements do not cover the geostrophic-turbulence state. The local maximum values of the spatial autocorrelations, see Figure 7(b), show a decrease with increasing $RaEk^{4/3}$ and they are practically zero for $RaEk^{4/3} \gtrsim 70$. The simulated values for the temperature autocorrelations are plotted as black stars and they show a reasonable agreement.

In conclusion, the spatial vorticity autocorrelations show similar trends as those of the spatial temperature autocorrelations calculated based on the asymptotically reduced equations. In addition, the spatial vorticity autocorrelation shows a change in the slope in the vicinity of $RaEk^{4/3} \simeq 70$ which is most probably due to the transition from the cellular-columnar state to the plume state. The results of the temporal vorticity autocorrelations are discussed in the Appendix.

1. Effects of Ekman number on the correlations

The experimental data, see Figures 6(a)–6(d), show that the blue symbols (experiments with variation in the background rotation) are generally lower than the red symbols (experiments with variation in the temperature difference) for similar $RaEk^{4/3}$ values. Exploring Tables I and II reveals that the blue data points possess relatively higher Ek. In other words, for two experimental data sets with an equal $RaEk^{4/3}$ value, the dimensionless spatial vorticity autocorrelation is wider for the data set with a smaller Ek number. The measurement for $RaEk^{4/3} = 55$ clearly manifests the effects of large Ek since it possesses the largest Ek in our data sets.

We examine four different points from both the PIV and the 3D-PTV measurements, viz., those with $RaEk^{4/3} = 27, 32, 55$, and 67; see Tables I and II for details. A true comparison should be drawn between these points and their limiting case counterparts where $Ek \to 0$. However, here the limiting case data are not available; therefore, the points with large Ek are compared with the data points with smaller Ek (based on the availability of the experimental data). The experimental data points with smaller Ek are only available for different $RaEk^{4/3}$ values and thus an interpolation or extrapolation is required. For example, the autocorrelation values for the measurement at $RaEk^{4/3} = 55$ ($Ek = 12.3 \times 10^{-6}$-large Ek) are compared with the interpolated values (linear interpolation) based on the measurements at $RaEk^{4/3} = 50$ ($Ek = 2.84 \times 10^{-6}$) and $RaEk^{4/3} = 63$ ($Ek = 2.77 \times 10^{-6}$). Therefore, we have two experimental data points with the same $RaEk^{4/3}$ but different Ek; for the aforementioned example, we have $RaEk^{4/3} = 55$ and $Ek = 12.3 \times 10^{-6}$ for Ek^{large} and $RaEk^{4/3} = 55$ and $Ek = 2.8 \times 10^{-6}$ for Ek^{small}. Table III presents the Ek^{large} and Ek^{small} data for all considered cases.

As discussed before, L_c (which is a function of Ek) is used to nondimensionalize the separation distance in the spatial vorticity autocorrelations (d/L_c). Here, we compare the values of d/L_c for Ek^{large} with those of Ek^{small} for the half-width and first zero crossing. The ratio RA is defined as

$$RA = \frac{d/L_c(Ek^{small})}{d/L_c(Ek^{large})},$$

where $d/L_c(Ek^{large})$ and $d/L_c(Ek^{small})$ are the data for the measurements with large and small Ek, respectively, and the same $RaEk^{4/3}$. Figure 8 shows the ratio RA at the half-width and first zero crossing as a function of Ek^{large}/Ek^{small}. The points in the plot from the smallest Ek^{large}/Ek^{small} to the largest Ek^{large}/Ek^{small} (left to right) correspond to $RaEk^{4/3} = 67$, 27, 32, and 55, respectively, see Table III as well. Note that d/L_c is dimensionless and it does not explicitly give information on the physical width of the structures. The ratio RA shows an increase with Ek^{large}/Ek^{small} indicating that dimensionless structures become smaller with increasing Ek when $RaEk^{4/3}$ is maintained constant. While the asymptotic equations do not explicitly depend on Ek and $RaEk^{4/3}$ is used as a parameter for description of the flow dynamics, we thus observed a dependency of the flow dynamics on the Ekman number for constant $RaEk^{4/3}$. However, it should be noted that this dependency is small; e.g., if the Ekman number increases by a factor of 5,

TABLE III. Ek^{large} and Ek^{small} data for all considered cases. Ek^{small} represents the interpolated data.

Ek^{large}/Ek^{small}	1.2	2.3	2.7	4.4
$RaEk^{4/3}$	67	27	32	55
$Ek^{large} \times 10^6$	3.42	7.03	8.20	12.30
$Ek^{small} \times 10^6$	2.83	3.10	3.07	2.80

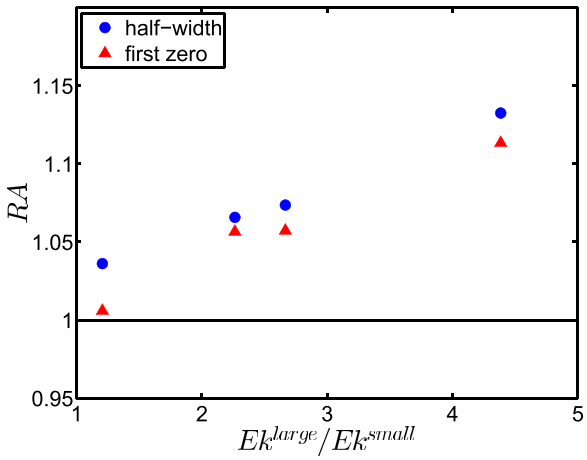

FIG. 8. The ratio RA for different Ek^{large}/Ek^{small}, indicating the effects of Ek on the length scales inferred from the correlations. The blue circles and red triangles show the ratio RA calculated for half-width and first zero crossing of the spatial vorticity autocorrelations, respectively.

the typical dimensionless coherency length scale decreases by approximately 13%.

The physical width of the structure shows the opposite behavior and it increases with Ek (as expected). Based on the definition of L_c, it increases as $L_c \propto Ek^{1/3}$. The physical width of the autocorrelation increases as well but at a smaller rate. Therefore, the ratio RA shows an increase with increasing Ek.

B. Flow coherence along the rotation axis

Up to now, we examined the spatial vorticity autocorrelations at $z = 0.8H$ for the entire plane consisting of the plumes (columns) and the intervening regions. However, in this section the coherent structures (plumes or columns) are examined separately from the regions between the columns or plumes. For this purpose, we are first required to detect the region populated by the plumes (columns). A widely used method for the vortex detection is the so-called Q-criterion method.[37] For a three-dimensional flow field a vortex is defined as a spatial region where

$$Q = \frac{1}{2}(||\tilde{\mathbf{\Omega}}||^2 - ||\mathbf{S}||^2) > 0, \tag{7}$$

with $\tilde{\mathbf{\Omega}}$ and $\mathbf{S}$ the antisymmetric and symmetric parts of the velocity gradient tensor, respectively. In this equation, the operator $||\mathbf{A}||$ is the Euclidean norm

$$||\mathbf{A}|| = \sqrt{\mathrm{Tr}\,(\mathbf{A}\mathbf{A}^T)}. \tag{8}$$

Figure 9 shows snapshots of the isosurfaces of $Q = 0.5Q_{rms}$, where Q_{rms} is the root mean square of Q at the time of the snapshot. This threshold is introduced only for the purpose of a better illustration. The isosurfaces are plotted for three different cases: weakly rotating Rayleigh–Bénard turbulence, plume state, and cellular state. Figure 9(a) shows the isosurface of Q for a weakly rotating Rayleigh–Bénard turbulence case ($RaEk^{4/3} = 3644$ and $Pr = 6.7$). As can be seen from the figure, there are no clear vertical correlations for this case. In Figure 9(b), the vertically aligned plumes become apparent for $RaEk^{4/3} = 120$ (plume state). For small values of $RaEk^{4/3}$, see Figure 9(c) for $RaEk^{4/3} = 18$, the cells are the main features of the flow. The blue and red colored surfaces represent the down-going (cold) and up-going (hot) plumes (columns), respectively.

The first parameter we examine is the variation of the vorticity along the axis of rotation. Figure 10 shows the color plot of the vorticity autocorrelation along the rotation axis. The starting point of the autocorrelation is located at $z = 0.96H$ and the final point is at $z = 0.762H$. The autocorrelation is calculated only in the points where the condition $Q > 0$ at $z = 0.96H$ is satisfied. As can be seen from the graph, a gradual decrease in the coherence is observable. The simulations show similar trends.[6] However, they found more coherence for small $RaEk^{4/3}$ values and less coherence for large $RaEk^{4/3}$ values compared to the experiments. Note that the sign of vorticity will flip as we move down far enough in a column;[38,39] the vortical plumes spin down as they approach the center. This property dictates a gradual decrease in the vorticity value (decorrelation) regardless of the $RaEk^{4/3}$ values. Hence, another criterion which does not depend on the height is more appropriate. Thus, a binary function A is introduced as

$$A = \begin{cases} 1, & \text{if } Q > 0, \\ 0, & \text{otherwise.} \end{cases} \tag{9}$$

The gradual decrease in the vertical vorticity value is not reflected in the binary function A. Thus, A is a more suitable representative of how far the plumes (columns) extend into the bulk.

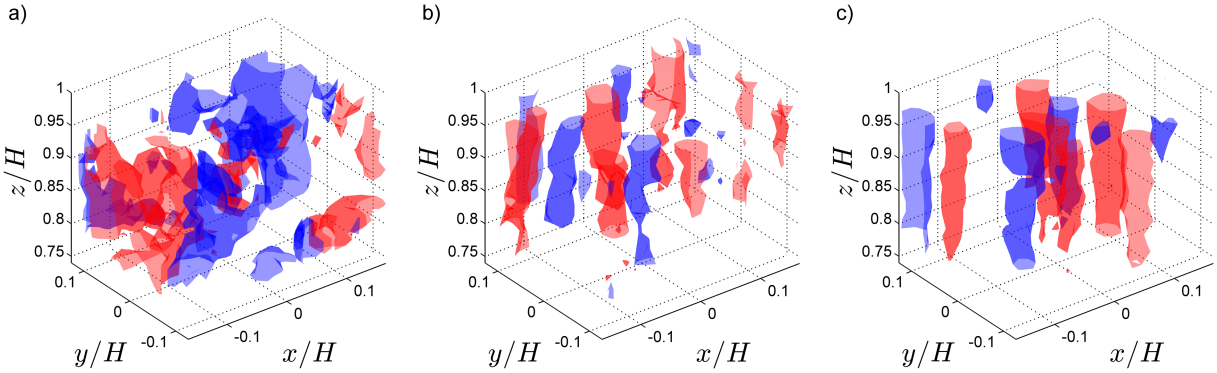

FIG. 9. Isosurfaces of Q for (a) $RaEk^{4/3} = 3644$ (weakly rotating Rayleigh–Bénard turbulence, $Ek = 6.8 \times 10^{-5}$, $Ra = 1.3 \times 10^9$ and $Pr = 6.7$), (b) $RaEk^{4/3} = 120$, and (c) $RaEk^{4/3} = 18$. The blue surfaces represent the cold plumes and red are the hot plumes.

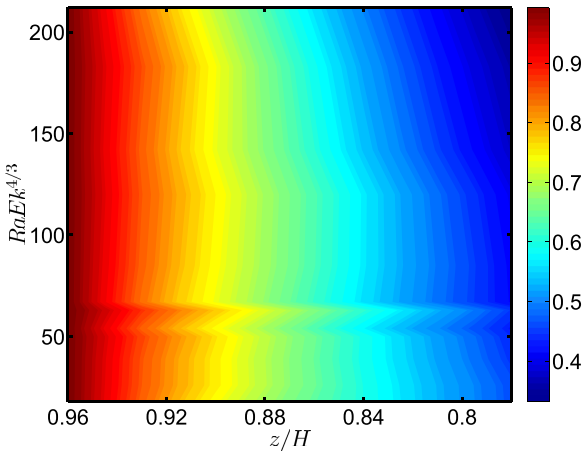

FIG. 10. Color plot of the autocorrelation of the vorticity as a function of height for different $RaEk^{4/3}$ values. The "spike" in the plot at $RaEk^{4/3} = 63$ depicts a stronger correlation than the adjacent values, but it is still within the accuracy range.

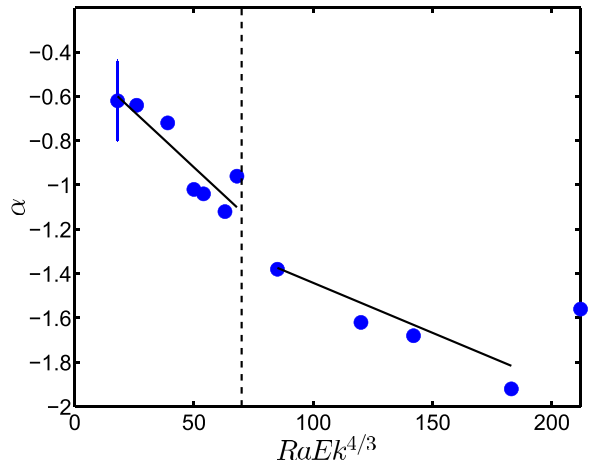

FIG. 12. The slopes α of the linear fit $R_A^z = \alpha \frac{z}{H} + \gamma$ to the autocorrelation of A as a function of $RaEk^{4/3}$. The dashed black line is located at $RaEk^{4/3} = 70$ and the solid black lines are guides to the eye through the experimental data points for $RaEk^{4/3} \lesssim 70$ and $RaEk^{4/3} \gtrsim 70$.

The autocorrelation of the binary function A is plotted in Figure 11. The vertical axis represents the autocorrelation coefficient and the horizontal axis is z/H, where $z/H = 1$ is at the top plate. The horizontal axis starts at $z = 0.96H$ since the autocorrelation is calculated only on the points starting at $z = 0.96H$. It can be seen that there is a rather abrupt drop down to $z = 0.92H$ and then the autocorrelation shows an approximately linear decay. The first abrupt drop is a direct consequence of the measurement noise. In other words, the Q-criterion approach identifies some points as a vortex (the binary number for a vortex region is 1) which become uncorrelated (the binary number for a non-vortex region is 0) at short distances. The effect of the noise vanishes for larger distances.

It is possible to fit a line $R_A^z = \alpha \frac{z}{H} + \gamma$ to the part where the autocorrelation shows a linear decay and take the slope α as the decay rate at which the plumes become uncorrelated. Figure 12 shows α as a function of $RaEk^{4/3}$. Note that $\alpha = 0$ indicates a fully vertically correlated flow field. The α values in Figure 12 are compatible with the transition observed at $RaEk^{4/3} \simeq 70$; the decay rate of the slope as a function of $RaEk^{4/3}$ is larger for $RaEk^{4/3} \lesssim 70$ compared to that for $RaEk^{4/3} \gtrsim 70$. Note that α decreases with increasing $RaEk^{4/3}$, indicating that the flow coherence along the axis of rotation decreases with increasing $RaEk^{4/3}$.

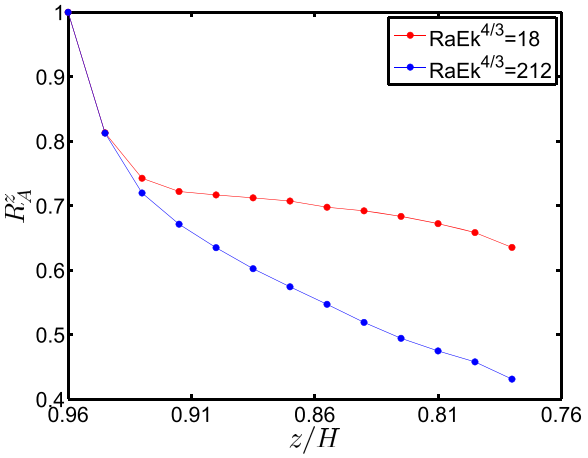

FIG. 11. Autocorrelation of the binary function A for $RaEk^{4/3} = 18$ and 212.

IV. CONCLUSIONS

We have explored the geostrophic regime of rapidly rotating turbulent convection with laboratory experiments based on classical tools: a table-top convection cell with a height of 0.2 m filled with water as the working fluid. We use two different optical flow diagnostic techniques: 3D-PTV and time-resolved PIV.

We pushed the boundaries of our experimental setting to determine if and how far we can enter the geostrophic regime of rapidly rotating convention using a conventional Rayleigh–Bénard convection cell. To achieve this goal, we compare our experimental data of the spatial vorticity autocorrelations with the spatial temperature autocorrelations from the simulations of the asymptotic equations, taken from Ref. 8. Surprisingly, most of the reported observations are well reflected in our experimental dataset. This is not guaranteed *a priori* as we deal with an experiment with boundary layers on top, bottom, and sidewalls and inevitably nonideality (e.g., heat loss and centrifugal buoyancy), in comparison to simulations with stress-free conditions at the plates and no sidewall.

The dependence of the spatial autocorrelations on Ek is investigated. It is observed that the spatial vorticity autocorrelations are different for two data sets with equal $RaEk^{4/3}$ but different Ek. Our findings show that the width of the (dimensionless) spatial vorticity autocorrelation becomes smaller with increasing Ek. It is worth pointing out that the physical (dimensional) width of the autocorrelation actually increases with Ek. Finally, the autocorrelations of the vorticity (and a binary function based on the Q-criterion) along the axis of rotation are examined. The results show an increase in the vertical coherence with decrease in $RaEk^{4/3}$.

We show that we can indeed reach the geostrophic regime of rapidly rotating convection using conventional convection cells. Furthermore, these experimental data provide support for the asymptotic approach. We find a good agreement

between experimental and simulation data by examining different parameters and we show that it is possible to reproduce the basic signatures of the asymptotic solutions in an experiment. This proves that we can definitely learn more from the asymptotically reduced equations and further attention to this theory in the rapidly rotating convection community is encouraged.

We are currently developing a rotating four-meter-tall convection cell combined with a stereoscopic PIV system which enables further exploration of the geostrophic regime and will allow for more extensive comparisons to the asymptotic simulations.

ACKNOWLEDGMENTS

This work is supported by the Nederland Wetenschappelijk Onderzoek (NWO), the Netherlands—formerly known as Stichting voor Fundamenteel Onderzoek der Materie (FOM). R.P.J.K. has received funding from the European Research Council (ERC) under the European Union's Horizon 2020 research and innovation programme (Grant Agreement No. 678634). The authors would like to express special thanks of gratitude to Ad Holten, Gerald Oerlemans, and Freek van Uittert for assisting with the preparation of the experimental setup.

APPENDIX: TEMPORAL VORTICITY AUTOCORRELATION

As discussed in Sec. III A, the spatial vorticity autocorrelation can be employed to study the geostrophic regime. Therefore, it is expected that the temporal vorticity autocorrelation also provides insight into the geostrophic regime. The temporal vorticity autocorrelation is defined as

$$R_\omega^\tau(\tau) = \frac{\langle \omega(x,y,z,t)\omega(x,y,z,t+\tau)\rangle}{\langle \omega^2(x,y,z,t)\rangle}, \qquad \text{(A1)}$$

where τ is the time lag. The temporal vorticity autocorrelation is plotted in Figure 13(a) as a function of τ and $RaEk^{4/3}$. The horizontal axis is nondimensionalized by the buoyancy time scale T_b, see Tables I and II. The temporal vorticity autocorrelations show a faster decorrelation with increasing $RaEk^{4/3}$. Similar behavior is observed in Ref. 8 for temperature autocorrelations. Figure 13(b) shows the dimensionless values of the half-width of the temporal vorticity autocorrelations (T_{hw}) as a function of $RaEk^{4/3}$. The data from the simulations show noticeably larger T_{hw} (the simulation data are not shown here, see Ref. 8 for more details), approximately six times larger than those of the experiments; the reason behind this discrepancy is not known. However, simulations show similar trends for the temporal autocorrelation as those of the experiments. Similar to the spatial autocorrelation, a change in the slope occurs in the vicinity of $RaEk^{4/3} \simeq 70$.

Nieves *et al.* used the temporal autocorrelation as an indication of how long it takes for a coherent structure to pass through a fixed point in space, i.e., the temporal autocorrelation can also be expressed as the velocity of a coherent structure (U_{coh}) divided by its width. Therefore, the velocity of a coherent structure can be written as the half-width of the spatial vorticity autocorrelation (L_{hw}) divided by the half-width of the temporal vorticity autocorrelation;[8] $U_{coh} = L_{hw}/T_{hw}$. Figure 14 shows U_{coh}/u_{rms}, where u_{rms} is the root-mean-square of the horizontal velocity fluctuations, $u_h = \sqrt{u_x^2 + u_y^2}$ with u_x and u_y the velocity components in the x and y directions, respectively. As can be seen from the graph, the ratio U_{coh}/u_{rms} becomes larger with increase in $RaEk^{4/3}$. The simulations are plotted as black stars in Figure 14 and they show a decent agreement for $RaEk^{4/3} \lesssim 100$. Note that the numerical data for $RaEk^{4/3} = 140$ from the simulations are for the geostrophic-turbulence state ($Pr = 1$), so no quantitative agreement is to be expected.

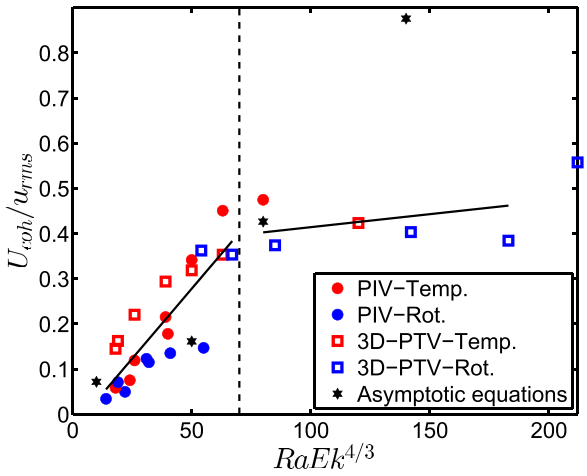

FIG. 14. U_{coh}/u_{rms} as a function of $RaEk^{4/3}$. The dashed black line is located at $RaEk^{4/3} = 70$ and the solid black lines are guides to the eye through the experimental data points for $RaEk^{4/3} \lesssim 70$ and $RaEk^{4/3} \gtrsim 70$.

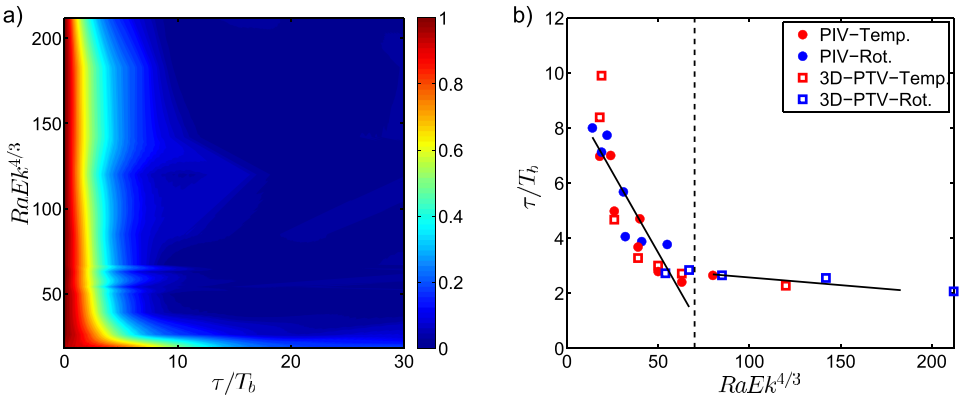

FIG. 13. (a) Color plot of the temporal vorticity autocorrelation from the 3D-PTV data as a function of $RaEk^{4/3}$ and (b) the half width of the temporal vorticity autocorrelation from 3D-PTV and PIV divided by the buoyancy time scale T_b (see Table I) as a function of $RaEk^{4/3}$. The dashed black line is located at $RaEk^{4/3} = 70$ and the solid black lines are guides to the eye through the experimental data points for $RaEk^{4/3} \lesssim 70$ and $RaEk^{4/3} \gtrsim 70$.

To summarize, although the experimental data show a faster temporal decorrelation (faster flow motions) than simulations, the ratio of U_{coh}/u_{rms} shows a good match with the simulation data.

[1] F. H. Busse and C. R. Carrigan, "Laboratory simulation of thermal convection in rotating planets and stars," Science **191**, 81–83 (1976).
[2] F. H. Busse, "Convection driven zonal flows and vortices in the major planets," Chaos **4**, 123–134 (1994).
[3] J. Marshall and F. Schott, "Open-ocean convection: Observations, theory, and models," Rev. Geophys. **37**, 1–64, doi:10.1029/98rg02739 (1999).
[4] K. Julien, E. Knobloch, and J. Werne, "A new class of equations for rotationally constrained flows," Theor. Comput. Fluid Dyn. **11**, 251–261 (1998).
[5] M. Sprague, K. Julien, E. Knobloch, and J. Werne, "Numerical simulation of an asymptotically reduced system for rotationally constrained convection," J. Fluid Mech. **551**, 141–174 (2006).
[6] K. Julien, A. M. Rubio, I. Grooms, and E. Knobloch, "Statistical and physical balances in low Rossby number Rayleigh–Bénard convection," Geophys. Astrophys. Fluid Dyn. **106**, 392–428 (2012).
[7] K. Julien, E. Knobloch, A. M. Rubio, and G. M. Vasil, "Heat transport in low-Rossby-number Rayleigh-Bénard convection," Phys. Rev. Lett. **109**, 254503 (2012).
[8] D. Nieves, A. M. Rubio, and K. Julien, "Statistical classification of flow morphology in rapidly rotating Rayleigh-Bénard convection," Phys. Fluids **26**, 086602 (2014).
[9] S. Stellmach, M. Lischper, K. Julien, G. Vasil, J. S. Cheng, A. Ribeiro, E. M. King, and J. M. Aurnou, "Approaching the asymptotic regime of rapidly rotating convection: Boundary layers versus interior dynamics," Phys. Rev. Lett. **113**, 254501 (2014).
[10] A. M. Rubio, K. Julien, E. Knobloch, and J. B. Weiss, "Upscale energy transfer in three-dimensional rapidly rotating turbulent convection," Phys. Rev. Lett. **112**, 144501 (2014).
[11] K. Julien, J. M. Aurnou, M. A. Calkins, E. Knobloch, P. Marti, S. Stellmach, and G. M. Vasil, "A nonlinear model for rotationally constrained convection with Ekman pumping," J. Fluid Mech. **798**, 50–87 (2016).
[12] M. Plumley, K. Julien, P. Marti, and S. Stellmach, "The effects of Ekman pumping on quasi-geostrophic Rayleigh–Bénard convection," J. Fluid Mech. **803**, 51–71 (2016).
[13] H. T. Rossby, "A study of Bénard convection with and without rotation," J. Fluid Mech. **36**, 309–335 (1969).
[14] F. Zhong, R. E. Ecke, and V. Steinberg, "Rotating Rayleigh–Bénard convection: Asymmetric modes and vortex states," J. Fluid Mech. **249**, 135–159 (1993).
[15] Y. Liu and R. E. Ecke, "Heat transport scaling in turbulent Rayleigh-Bénard convection: Effects of rotation and Prandtl number," Phys. Rev. Lett. **79**, 2257 (1997).
[16] E. M. King, S. Stellmach, J. Noir, U. Hansen, and J. M. Aurnou, "Boundary layer control of rotating convection systems," Nature **457**, 301–304 (2009).
[17] Y. Liu and R. E. Ecke, "Heat transport measurements in turbulent rotating Rayleigh-Bénard convection," Phys. Rev. E **80**, 036314 (2009).
[18] J.-Q. Zhong, R. J. A. M. Stevens, H. J. H. Clercx, R. Verzicco, D. Lohse, and G. Ahlers, "Prandtl-, Rayleigh-, and Rossby-number dependence of heat transport in turbulent rotating Rayleigh-Bénard convection," Phys. Rev. Lett. **102**, 044502 (2009).
[19] S. Weiss, R. J. A. M. Stevens, J.-Q. Zhong, H. J. H. Clercx, D. Lohse, and G. Ahlers, "Finite-size effects lead to supercritical bifurcations in turbulent rotating Rayleigh-Bénard convection," Phys. Rev. Lett. **105**, 224501 (2010).
[20] J.-Q. Zhong and G. Ahlers, "Heat transport and the large-scale circulation in rotating turbulent Rayleigh–Bénard convection," J. Fluid Mech. **665**, 300–333 (2010).
[21] R. P. J. Kunnen, R. J. A. M. Stevens, J. Overkamp, C. Sun, G. J. F. van Heijst, and H. J. H. Clercx, "The role of Stewartson and Ekman layers in turbulent rotating Rayleigh–Bénard convection," J. Fluid Mech. **688**, 422–442 (2011).
[22] S. Weiss and G. Ahlers, "Heat transport by turbulent rotating Rayleigh–Bénard convection and its dependence on the aspect ratio," J. Fluid Mech. **684**, 407–426 (2011).
[23] S. Weiss and G. Ahlers, "The large-scale flow structure in turbulent rotating Rayleigh–Bénard convection," J. Fluid Mech. **688**, 461–492 (2011).
[24] S. Schmitz and A. Tilgner, "Heat transport in rotating convection without Ekman layers," Phys. Rev. E **80**, 015305 (2009).
[25] S. Schmitz and A. Tilgner, "Transitions in turbulent rotating Rayleigh-Bénard convection," Geophys. Astrophys. Fluid Dyn. **104**, 481–489 (2010).
[26] R. J. A. M. Stevens, H. J. H. Clercx, and D. Lohse, "Optimal Prandtl number for heat transfer in rotating Rayleigh–Bénard convection," New J. Phys. **12**, 075005 (2010).
[27] S. Horn and O. Shishkina, "Toroidal and poloidal energy in rotating Rayleigh–Bénard convection," J. Fluid Mech. **762**, 232–255 (2015).
[28] R. E. Ecke and J. J. Niemela, "Heat transport in the geostrophic regime of rotating Rayleigh-Bénard convection," Phys. Rev. Lett. **113**, 114301 (2014).
[29] J. S. Cheng, S. Stellmach, A. Ribeiro, A. Grannan, E. M. King, and J. M. Aurnou, "Laboratory-numerical models of rapidly rotating convection in planetary cores," Geophys. J. Int. **201**, 1–17 (2015).
[30] R. P. J. Kunnen, R. Ostilla-Mónico, E. P. van der Poel, R. Verzicco, and D. Lohse, "Transition to geostrophic convection: The role of the boundary conditions," J. Fluid Mech. **799**, 413–432 (2016).
[31] S. Chandrasekhar, *Hydrodynamic and Hydromagnetic Stability* (Oxford University Press, 1961).
[32] E. M. King, S. Stellmach, and J. M. Aurnou, "Heat transfer by rapidly rotating Rayleigh–Bénard convection," J. Fluid Mech. **691**, 568–582 (2012).
[33] R. P. J. Kunnen, B. J. Geurts, and H. J. H. Clercx, "Experimental and numerical investigation of turbulent convection in a rotating cylinder," J. Fluid Mech. **642**, 445–476 (2010).
[34] R. P. J. Kunnen, Y. Corre, and H. J. H. Clercx, "Vortex plume distribution in confined turbulent rotating convection," Europhys. Lett. **104**, 54002 (2014).
[35] H. Rajaei, P. Joshi, K. M. J. Alards, R. P. J. Kunnen, F. Toschi, and H. J. H. Clercx, "Transitions in turbulent rotating convection: A Lagrangian perspective," Phys. Rev. E **93**, 043129 (2016).
[36] H. Rajaei, P. Joshi, R. P. J. Kunnen, and H. J. H. Clercx, "Flow anisotropy in rotating buoyancy-driven turbulence," Phys. Rev. Fluids **1**, 044403 (2016).
[37] J. C. R. Hunt, A. A. Wray, and P. Moin, "Eddies, streams, and convergence zones in turbulent flows," Report No. CTR-S88, Center for Turbulence Research, 1988.
[38] J. W. Portegies, R. P. J. Kunnen, G. J. F. van Heijst, and J. Molenaar, "A model for vortical plumes in rotating convection," Phys. Fluids **20**, 066602 (2008).
[39] I. Grooms, K. Julien, J. B. Weiss, and E. Knobloch, "Model of convective Taylor columns in rotating Rayleigh-Bénard convection," Phys. Rev. Lett. **104**, 224501 (2010).